RESEARCH ARTICLE

ADVANCED
INTELLIGENT
SYSTEMS
Open Access

www.advintellsyst.com

Aggregation Volume Estimator–Based Offline Programming Guidance of Magnetic Nanoparticles in the Realistic Rat-Brain Vasculature Model

Myungjin Park, Seungjun Oh, Tuan Anh Le, and Jungwon Yoon*

Targeted delivery of magnetic nanoparticles (MNPs) to an area of a blood vessel with fluidic flow is hampered by the lack of a suitable real-time imaging modality for MNPs, the control system complexity, and low targeting performance. Herein, an offline programming guidance (OLPG) scheme for aggregated MNPs is proposed based on a real-time aggregation volume estimator. The proposed aggregation volume estimator based on a magnetic drug-targeting simulator reflects volume changes of aggregated MNPs; hence, it can model a magnetic force acting on aggregated MNPs in real time while enhancing targeting performance. The proposed guidance system is evaluated using a simulation testbed and in vitro model of the rat brain, which yields comparable results at different fluid viscosities, flow velocities, target areas, and flow types. The OLPG with the aggregation volume estimator improves targeting performance by 116%–409% compared with the default mode, and by 111%–180% compared to the performance without the aggregation volume estimator. Furthermore, a guidance margin predicts enhanced targeting performance (root-mean-square error < 5%) irrespective of the flow environment. The proposed guidance strategy has the potential to overcome the problems caused by the lack of an imaging modality, control-system complexity, and low targeting performance.

1. Introduction

Targeted drug delivery is becoming increasingly important for noninvasive treatment[1,2] because it enables targeted release of therapeutics at the site of disease.[3] Targeted drug delivery can involve in vivo biomedical[4] and physical drug-release mechanisms,[5] implantable systems,[6] and nanocarriers.[7] Multiple means of drug targeting have been proposed, including methods based on light, electricity, ultrasound, and magnetic fields.[8–10] Magnetic drug targeting (MDT) is safe and has good penetration.[11] However, implementing MDT using micro/nanorobots is a challenge.[12] The small propulsion force of micro/nanorobots hampers their control in dynamic flow environments, such as blood. However, aggregation and swarm control of micro/nanorobots can enhance the actuation force.[13,14]

Li et al. suggested a magnetic resonance navigation method using 200 μm magnetic drug-eluting beads (MDEBs) composed of Fe_3O_4 superparamagnetic nanoparticles (5–20 nm).[15] The induced magnetic force on a single Fe_3O_4 superparamagnetic nanoparticle is insufficient to steer it in a blood vessel, but MDEBs can increase the velocity of aggregated particles, allowing them to be guided to the desired outlet in a two-level bifurcation phantom. Vartholomeos et al. reported that aggregation enhances the propulsion efficiency of magnetic nanoparticles (MNPs) and achieved a targeting performance of ≈98%[16] in a Y-channel using a gradient field of 0.3 T m^{-1}. Wang et al. used a rotating permanent magnet to generate and move microswarms in an ex vivo blood vessel under fluidic flow.[17] However, the generation and guidance of micro/nanorobot swarms in 3D blood vessels are hampered by the lack of a suitable real-time imaging modality and 3D locomotion methods, insufficient dispersion characteristics, and the complexity of guidance.[18]

In robotics, offline programming (OLP)[19] generates complex control commands using a computer simulator calibrated to simulate a real environment without imaging sensors. OLP can generate complex control commands to guide micro/nanorobots to a target area through blood vessels without real-time imaging. In our prior study of OLP in MDT,[20] we assumed that MNPs aggregate only in their initial state, that is, not during MDT. As a result, the aggregate volume was considered to be constant. However, the aggregation volume of MNPs changed during MNP guidance in blood vessels according to the flow velocity, fluid viscosity, and magnetic field. Changes in MNP aggregation volume may promote errors between the real MDT environment

M. Park, S. Oh, J. Yoon
School of Integrated Technology
Gwangju Institute of Science and Technology Institute of Integrated Technology
123 Cheomdan Gwagiro, Gwangju 61005, Republic of Korea
E-mail: jyoon@gist.ac.kr

T. Anh Le
Department of Physiology and Biomedical Engineering
Mayo Clinic Scottsdale
13400 E Shea Blvd, Scottsdale, AZ 85259, USA

The ORCID identification number(s) for the author(s) of this article can be found under https://doi.org/10.1002/aisy.202300128.

**ADVANCED
SCIENCE NEWS**

www.advancedsciencenews.com

**ADVANCED
INTELLIGENT
SYSTEMS**

www.advintellsyst.com

and MDT simulator, thereby affecting MNP-targeting performance. Therefore, any change in the aggregated MNP volume in a real MDT environment needs to be reflected in the MDT simulator in real time. Furthermore, we verified an OLP scheme in a 2D artificial vascular model with a flow velocity of 5 mm s^{-1} and viscosity of 4 cP. However, the proposed guidance scheme was not validated in real blood vessels of various diameters, the model is 3D, the surface is not flat, and red blood cells (RBCs) are present.

Tracking of aggregated MNP volume would enable prediction of aggregation in real time without the need to calculate the interaction forces among MNPs. In this article, we propose a real-time aggregation volume estimator to predict MNP aggregation volume in blood vessels. The aggregation volume estimator reduces modeling errors between the MDT simulator and real MDT environment using the MDT flow velocity, fluid viscosity, and magnetic field strength. Furthermore, we propose a guidance margin to predict the enhancement ratio of targeting performance using the magnetic properties of MNPs, an aggregation volume estimator, magnetic field strength, fluid viscosity, and flow velocity in blood vessels. Calculating the guidance margin at the MDT simulator enables the calculation of targeting performance enhancement.

We verified the feasibility of the proposed guidance scheme in a model blood vessel using different viscosities (1.75–5.75 cP), fluids (glycerol mixtures and blood), and flow velocities (1–5 mm s^{-1}). The 3D geometry of the blood vessel was extracted from the magnetic resonance angiography (MRA) image of a rat brain. To implement 3D locomotion, we used fluid flow as a 1D control source and electromagnetic fields as a 2D control source. The proposed OLP guidance (OLPG) scheme with the aggregation volume estimator was evaluated in a model blood vessel; the results indicated the in vivo potential of the proposed OLPG scheme. Section 2 describes the aggregation volume estimator–based OLPG system, and Section 3 outlines the aggregation volume estimator (including real-time volume estimation of aggregated MNPs and experimental verification) and introduces the guidance margin concept. Section 4 describes the results of the proposed OLPG scheme in a simulation testbed (COMSOL) and in vitro, and its enhancement ratio of targeting performance in a simulation testbed and in vitro. Section 5 discusses the potential for in vivo application. The conclusions are provided in Section 6.

2. Aggregation Volume Estimator–Based OLPG Method

The aggregation volume estimator–based OLPG method for MNPs has an offline mode (MDT simulator) and an online mode (real environment) (**Figure 1**a). In the MDT simulator, the user generates control commands for the guidance of MNPs using the 3D joystick (Phantom Omni), and the resultant forces applied to MNPs are calculated in MATLAB; their flow velocities in a vascular model were evaluated in COMSOL. Visual feedback on MNP positions is provided by Unity 3D. Control commands are downloaded to the PXI-controller (National Instruments) of the electromagnetic actuator (EMA) to guide MNPs to the target area via the bloodstream.

Herein, we define the center point of a swarm of aggregated MNPs injected into a blood vessel as the center point of a swarm of a multilayer magnetic chain (SMMC), which acts as the user

control point in the MDT simulator. The MDT simulator has physics and graphics engines (Figure 1b). In the MDT simulator loop, SMMC center position data were transferred to physics engine I (COMSOL) and II (MATLAB) via UDP communication. The initial SMMC position was determined by calibration of the MDT simulator based on the in vitro environment.[20] The SMMC center position is updated by the physics engines during the operation of the MDT simulator. In physics engine I, the hydrodynamic force on SMMC is calculated from the flow velocity and viscosity at the SMMC center position by Livelink (COMSOL–MATLAB). Simultaneously, the SMMC flow velocity/viscosity was transferred to physics engine II, and the magnetic field and magnetic field gradient at the SMMC center position were calculated. This enabled calculation of SMMC volume (Figure 1c). SMMC can be modeled as a rod shape; hence, its volume can be calculated by multiplying the radial aggregation area and axial aggregation length (**Figure 2**a). The axial aggregation length can be mathematically modeled using the correlation between hydrodynamic drag force and magnetic dipolar energy.[21] The empirical equation for the radial aggregation area can be constructed by measuring the velocity of aggregated MNPs in vitro (calibration phase). Next, the SMMC volume can be estimated in real time using the radial aggregation area and the axial aggregation length (real-time phase). The aggregation volume estimator is described in detail in Section 3.

The total force applied to SMMC was calculated. The total applied force can change the SMMC center position at 30 Hz; this was transferred to the graphics engine, which displays the SMMC center position at 1 kHz. We introduced a guidance margin to estimate the enhancement of targeting performance in a real MDT environment (Figure 1d). During SMMC guidance with the MDT simulator, the guidance ratio, defined as the ratio between the contributed velocity component and the non-contributed velocity component into the guidance (Section 3.4), was calculated using the magnetic force, flow velocity, and hydrodynamic drag force. The guidance ratio when the SMMC begins to be guided to the target area was used as the critical guidance ratio. The guidance margin was defined as the difference between the guidance ratio and critical guidance ratio. When the SMMC reaches the target area, the guidance margin can be evaluated. The user can predict the guidance results using the relationship between the guidance margin and the enhancement ratio of targeting performance.

The guidance process is as follows. First, raw rat-whole-brain vasculature data were obtained by ultrashort echo time MRA (UTE–MRA).[22] The raw data were segmented using 3D Slicer (Kitware) and the internal carotid artery (ICA), middle cerebral artery (MCA), and anterior cerebral artery (ACA) were segmented (Figure 1e) for MDT. A 3D model of the segmented vasculature was transferred to the MDT simulator as an STereoLithography (STL) format file (Figure 1f). The vascular model was uploaded to COMSOL to simulate realistic fluidic flow. The flow velocity/viscosity information generated in COMSOL was transferred to Unity 3D, which generated SMMC with predefined magnetic properties and density; the SMMC volume was updated at 30 Hz by MATLAB. In the MDT simulator (Unity3D), the user-guided the SMMC center position to the target area and the control command was saved in the form of current intensity, which was downloaded to the EMA controller for MNP guidance (Figure 1g).
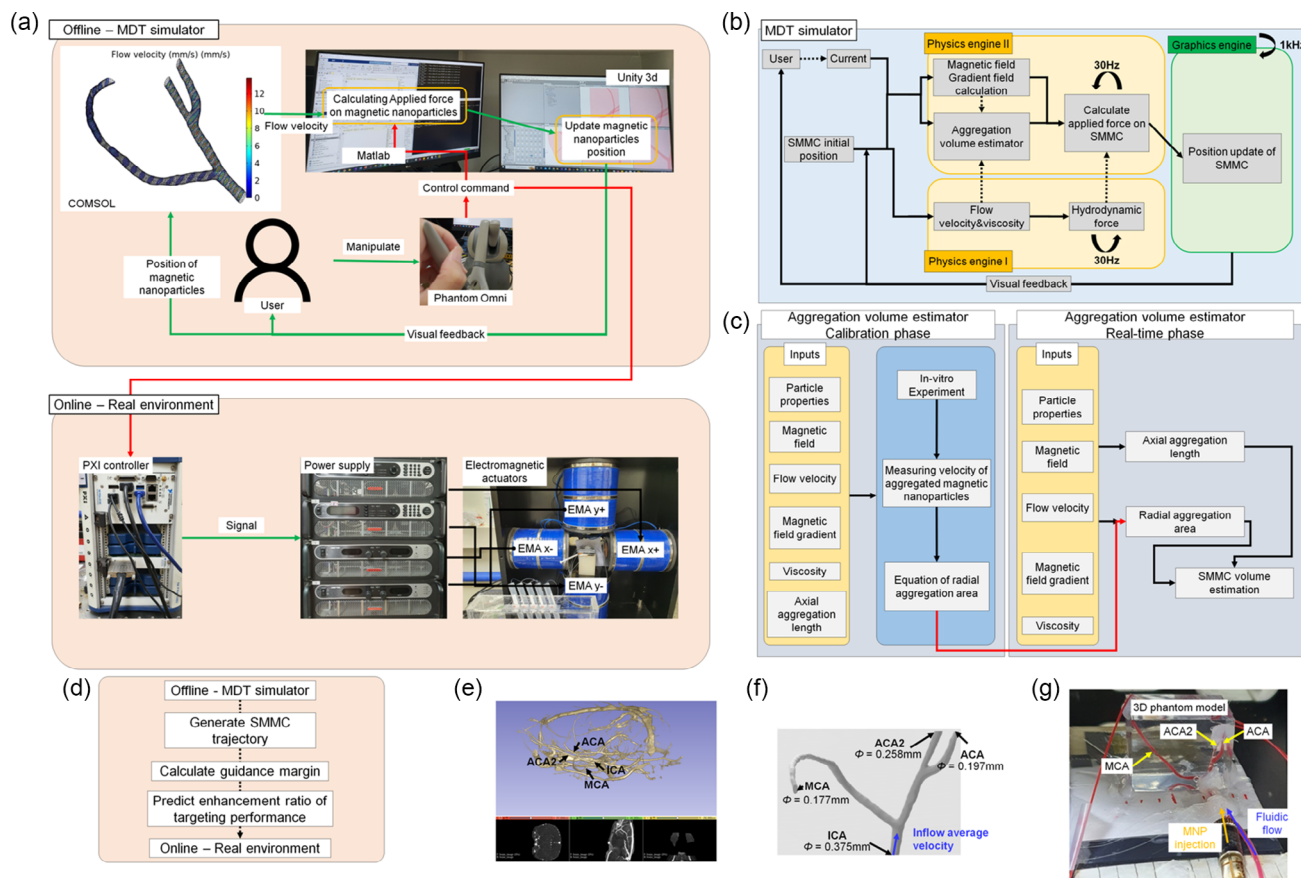
Figure 1. Aggregation model-based offline programming guidance (OLPG) system. a) Magnetic drug-targeting (MDT) simulator using a Phantom Omni joystick, COMSOL, MATLAB, and Unity3D. b) MDT simulator loop comprising physics and graphics engines. The total net forces on the swarm of a multilayer magnetic chain (SMMC) are calculated by the physics engine and SMMC positions are displayed by the graphics engine. c) Aggregation volume estimator comprising calibration and real-time phases. In the calibration phase, the empirical equation for radial aggregation area (radial) was determined in vitro, and the aggregation volume was calculated based on the axial aggregation length and radial aggregation area in the real-time phase. d) By calculating the guidance margin in the MDT simulator, the enhancement of targeting performance can be estimated. e) Extracts of a rat-brain vessel from the magnetic resonance angiography (MRA) data of a real rat-brain vessel, f) segmented specific vascular (internal carotid artery–middle cerebral artery–anterior cerebral artery [ICA–MCA–ACA]) from a rat-brain vessel, and g) in vitro 3D phantom model.

3. Design of the MNP Aggregation Volume Estimator

When a static magnetic field was applied, the MNPs aligned in the field direction and aggregated in chains. Ideally, aggregation increases only in the direction of the applied field (Figure 2a; single-layer magnetic chain), but it tends to increase in other directions in a 3D environment (Figure 2a; multilayer magnetic chain). Multilayer magnetic chain aggregation is divided into axial and radial aggregation (Figure 2b). We denote the magnetic field direction as axial and the direction perpendicular to the field as radial. Herein, we modeled the multilayer magnetic chain as a rod shape and the volume can be calculated by multiplying the axial aggregation length by the radial aggregation area. Specifically, the nanoparticles were randomly dispersed in water with no external magnetic field (Figure S15, Supporting Information [$t = 0$]). Once the discrete magnetic field was applied, the MNPs are aggregated as rod-shaped magnetic chains (Figure S15, Supporting Information ($t = 5s \approx t = 10s$)). When the applied

magnetic field is periodic, the axial aggregation length of SMMC was determined by the relationship between the magnetic torque and viscous torque (Mason number[23]). Because the applied magnetic field was discrete rather than periodic, SMMC aggregation was mainly restricted by the relationship between magnetic potential energy and viscous forces.[21] Consequently, the torque relations of the SMMC were not considered when the axial aggregation length was determined. Moreover, it should be taken into account that the interaction forces between MNPs and bio components (e.g., RBCs) are negligible under our experimental conditions, hence the aggregation between MNPs is only considered (Note S3, Supporting Information).

The dipole force is the dominant contributor to MNP aggregation.[24] However, it is impossible to induce aggregation in real time in an MDT simulator due to a large number of MNPs ($\approx 10^{12}$/g). Because MNP aggregation increases MNP aggregate volume,[25] MNP aggregation can be predicted by tracking the aggregation volume. As a result, the aggregation volume
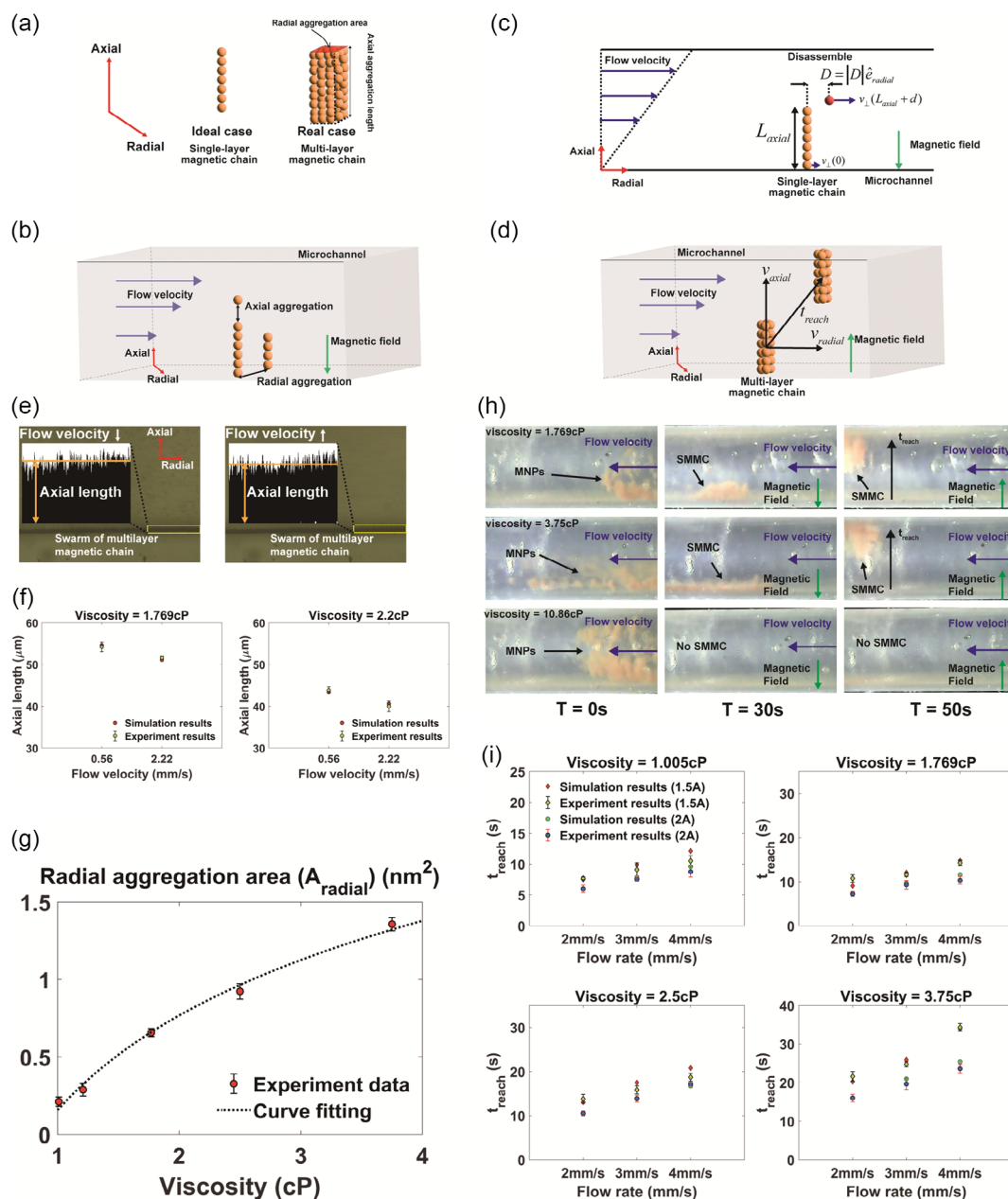
Figure 2. a–d) Analytic aggregation modeling and e–i) verification. a) Geometric shapes of ideal and real magnetic chains. b) Axial and radial aggregation of a single-layer magnetic chain. c) A magnetic particle (red) disassembles from a single-layer magnetic chain (orange) when the hydrodynamic drag force exceeds the magnetic dipolar energy. d) Radial aggregation area determined by measuring v_{axial}. The multilayer magnetic chain has two velocity components: radial velocity (v_{radial}; due to flow velocity) and axial velocity (v_{axial}; due to magnetic force). e) Axial length at different flow velocities: an increase of flow velocity restricts magnetic chain length; hence, the average axial length decreases. f) Measurement of average axial length and mathematical modeling of axial chain length. g) The radial aggregation area was determined by measuring the axial velocity of a swarm of multilayer magnetic chains (v_{axial} in (d)). h) Time (t_{reach}) required for a swarm of multilayer magnetic chains at the bottom wall to reach the top wall; a constant magnetic field was applied toward the bottom to reach equilibrium aggregation ($T = 30$ s). Thereafter, the opposite magnetic field was applied to measure the time required to reach the top wall ($T = 50$ s). i) Analysis of axial aggregation length (f) and radial aggregation area (g) allows calculation of aggregation volume. To validate the precision of the calculated volume, the t_{reach} values were compared.

estimator enables real-time MNP aggregation modeling by obviating the need to calculate MNP of interaction forces. In the following subsections, we validated the axial aggregation model and radial aggregation model by comparing them with experimental results, respectively. Finally, we identified the feasibility of the rod-shaped aggregation modeling with experimental results. To obtain reliable experimental results, we conducted this experiment three times.

**ADVANCED
SCIENCE NEWS**

www.advancedsciencenews.com

**ADVANCED
INTELLIGENT
SYSTEMS**
Open Access

www.advintellsyst.com

3.1. Axial Aggregation Length

Axial aggregation length can be determined by correlations between the dipole force and hydrodynamic drag force (Figure 2c). This can be analyzed based on the law of conservation of energy, where the work done by the flow equals the change in magnetic dipolar energy.

The average magnetic dipolar energy (U_m) between a single-layer magnetic chain and other MNPs in magnetic field B was calculated as follows

$$U_m = \sum_{i=1}^{1} \sum_{j=1}^{N} \frac{\mu_0}{4\pi r_{ij}^3} \left(3(m_i \cdot \hat{r}_{ij})(m_j \cdot \hat{r}_{ij}) - m_i \cdot m_j\right) \tag{1}$$

where i denotes additional particle i, and j is particle j in the single-layer magnetic chain, r is the distance between two particles, $\hat{r}$ is a unit vector parallel to the line joining the centers of the two dipoles, μ_0 is the permeability of air, m is the magnetic moment, and N is the number of MNPs in the single-layer magnetic chain. To calculate the magnetic moment (m), coupled Equations (2)–(4) should be solved by ref. [16]. The magnetic moment of particle i is

$$m_i = \frac{3V}{\mu_0} \left(\frac{\mu - \mu_0}{\mu + 2\mu_0}\right) B_i \tag{2}$$

where B_i is the total magnetic field on particle i, V is the volume of an individual MNP, and μ is the magnetic permeability. The total magnetic field can be represented as follows

$$B_i = B_{ext} + \sum_{j=1}^{N} B_{i,j} \tag{3}$$

where B_{ext} is the external magnetic field, and Σ indicates the accumulated magnetic field of adjacent MNPs.

The magnetic field of the ith particle with respect to jth is as follows

$$B_{i,j} = \frac{\mu}{4\pi} \left(\frac{3(m_j \cdot r_{ij})r_{ij}}{r_{ij}^5} - \frac{m_j}{r_{ij}^3}\right) \tag{4}$$

The magnetic moment of the ith MNP can be calculated by substituting Equations (3) and (4) into Equation (2). In this article, the magnetic moment induced by surrounding MNPs in Equation (4) was ignored. We assume that the total magnetic moment is equal to the sum of the magnetic moments of the individual MNPs.[25] This assumption is reasonable because the effect of an induced magnetic moment on total magnetic moment decreases as the external magnetic field strength increases (error < 5% at 50 mT).[25] As a result, the total magnetic moment (m) of the magnetic chain can be calculated as follows

$$m = N \frac{3V}{\mu_0} \left(\frac{\mu - \mu_0}{\mu + 2\mu_0}\right) B_{ext} \tag{5}$$

where N is the number of MNPs in the chain. The total magnetic moment of the magnetic chain is determined by substituting B_i with B_{ext} and V with NV into Equation (2). Equation (5) is used to derive the total magnetic moment (Equation (5)). The magnetic

moment is directly related to the magnetic dipolar energy (Equation (1)), which assists calculation of the magnetic dipolar energy in real time. Furthermore, because the magnetic dipolar energy (Equation (1)) decreases with increasing distance between MNPs ($\propto 1/r_{ij}^3$), the magnetic dipolar energy between MNPs can be ignored when the distance between them exceeds $10d$ (where d is the individual MNP diameter). Typically, the error will be <0.1% of that when the magnetic dipolar energies of all MNPs are considered.[25] This minimizes the computational load of calculating magnetic dipolar energy, thereby enabling real-time calculation.

Under fluid flow, the length of the magnetic chain is restricted by hydrodynamic drag forces. The magnetic chain grows until the hydrodynamic drag forces at the end of the magnetic chain exceed the magnetic dipole force. For instance (Figure 2c), a particle is released from the single-layer magnetic chain because the hydrodynamic drag force acting on it (red) exceeds the magnetic dipolar energy between it and the magnetic chain (orange).

Based on the modified Stokes law, the hydrodynamic drag force on the MNP at the end of the magnetic chain can be calculated as[26]

$$F_{drag} = 3\pi \eta d v_{\perp} \tag{6}$$

where η and d are the fluid viscosity and diameter of the individual MNP, respectively. The single-layer magnetic chain is affected by the flow velocity component of $v_{\parallel}$ and $v_{\perp}$, which are axial and radial, respectively. The axial flow velocity components can be ignored when analyzing axial aggregation because they do not contribute to chain disassembly. The magnetic field is always applied in the axial direction to maximize the interaction forces in that direction and the contribution of the flow velocity component in the axial direction is negligible compared to the interaction forces induced by the magnetic field. To determine magnetic chain length, the interaction between the single-layer magnetic chain and an MNP over the breaking displacement D should be considered (Figure 2c). Taking the derivative of the magnetic dipolar energy (Equation (1)) over the breaking displacement (D), the magnetic dipole force between an MNP and the magnetic chain can be calculated. The net dipole and hydrodynamic drag forces should be zero

$$\max\left(\frac{dU_m}{dD}\right) - 3\pi \eta d (v_{\perp}(L_{axial} + d) - v_{\perp}(0)) = 0 \tag{7}$$

Because the flow velocity profile in a channel is curved, it is highest at the centerline and zero at the walls.[27] The flow velocity profile can be fit empirically by

$$v_{\perp} = V_{max} \left(1 - \left(\frac{r}{R}\right)^{\varsigma}\right) \tag{8}$$

where $v_{\perp}$ is the flow velocity (m s^{-1}) in the radial direction, V_{max} is the maximum centerline flow velocity (m s^{-1}), r is the axial location of MNP, R is the radius of the channel (m), and ς is a constant for a particular profile. Magnetic chain axial length can be calculated by substituting Equation (8) into Equation (7)

$$L_{axial} = R - \left(d + R \sqrt[\varsigma]{1 - \frac{\max(\frac{dU_m}{dD})}{3\pi \eta d v_{\perp}}}\right) \tag{9}$$

To compare the axial aggregation length with the mathematical model (Equation (9)), we performed an in vitro experiment (Figure S1a, Supporting Information). In a microchannel, a multilayer magnetic chain is formed due to the dipole force and pulled to the channel bottom wall by the magnetic field gradient. Consequently (Figure 2e), a multilayer magnetic chain swarm is formed (SMMC = Σmultilayer magnetic chain). The average axial aggregation length of a multilayer magnetic chain swarm was measured using ImageJ (NIH).

As shown in Figure 2f, the SMMC average axial aggregation length was affected by the fluid viscosity and flow velocity. Higher viscosity increases the hydrodynamic drag force of (Equation (6)) and decreases the average SMMC axial length (Equation (9)). As flow velocity increases, MNPs experience higher flow velocity at the end of multilayer magnetic chain, which promotes MNP release from the multilayer magnetic chain. Moreover, the strength of the magnetic field effects on the axial aggregation length of multilayer magnetic chains (Figure S2, Supporting Information). Mathematical modeling of axial aggregation length yielded comparable trends to the experimental results (error < 0.5 μm) (Figure 2f). The difference was caused mainly by the nonuniform size of MNPs. In the simulation, MNPs are all 350 nm in diameter, whereas real MNPs are of various diameters with an average of 350 nm (Figure S3a, Supporting Information).

3.2. Radial Aggregation Area

In realistic situations, a single-layer magnetic chain can aggregate with another MNP or single-layer magnetic chain in the radial direction,[28] thereby forming a multilayer magnetic chain. To evaluate SMMC volume size, we determined the radial aggregation area (A_{radial}) in vitro. Previously, the average SMMC axial aggregation length (L_{axial}) was calculated by mathematical modeling (Section 3.1). The volume of a multilayer magnetic chain can be calculated as follows

$$V_{mmc} = L_{axial} A_{radial} \tag{10}$$

The volume of a multilayer magnetic chain (V_{mmc}) equals the sum of the volumes of the individual MNPs (NV). Substituting Equation (10) into Equation (5) shows that the total magnetic moment is proportional to L_{axial} and A_{radial}. The magnetic force increases with increasing magnetic moment. The magnetic force on a magnetic chain can be represented as

$$F_{mf} = \frac{3 V_{mmc}}{\mu_0} \left(\frac{\mu - \mu_0}{\mu + 2\mu_0} \right) (B_{ext} \cdot \nabla) B_{ext} \tag{11}$$

As inferred in Equation (11), radial aggregation area (A_{radial}) can be calculated if magnetic force is measured. Instead, we calculated the radial aggregation area by solving the net force Equation (12) of applied forces on MNPs. Because hydrodynamic drag, the magnetic field, and gravity are the main forces acting on MNPs (Section 7), the net force equation can be represented as follows

$$3\pi\eta d_e f_e v_{axial} - \frac{3 L_{axial} A_{radial}}{\mu_0} \left(\frac{\mu - \mu_0}{\mu + 2\mu_0} \right) (B_{ext} \cdot \nabla) B_{ext}$$
$$+ L_{axial} A_{radial} (\rho_{particle} - \rho_{fluid}) g = 0 \tag{12}$$

The effective diameter d_e is $L_{axial} E^{-2/3}$ ($E = L_{axial}/\sqrt{A_{radial}}$), the stoke correction factor f_e is $\frac{4/3 E^{2/3}}{\ln(2E) - 0.5}$,[26] v_{axial} is the axial velocity of multilayer magnetic chain, ρ_p is the particle density, ρ_f is the fluid density, and g is gravitational acceleration. Equation (12) calculates the radial aggregation area A_{radial} as follows

$$A_{radial} = \frac{3\pi\eta d_e f_e v_{axial}}{L_{axial} \left(\frac{3}{\mu_0} \left(\frac{\mu - \mu_0}{\mu + 2\mu_0} \right) (B_{ext} \cdot \nabla) B_{ext} - (\rho_p - \rho_f) g \right)} \tag{13}$$

Axial velocity (v_{axial}) is measured by image processing (MATLAB) after applying magnetic force toward the axial direction, the radial aggregation area (A_{radial}) can be determined as in Figure 2d. In realistic situations, axial velocity cannot be obtained because of the lack of a suitable real-time imaging modality, which hampers calculation of axial aggregation area by Equation (13). Through Equations (9) and (11), Equation (13) can be simply redefined as a fluid viscosity related equation. Compared with the axial direction, a negligible magnetic field is applied in the radial direction. Therefore, Brownian motion is more significant compared to the dipole force when determining the radial aggregation of MNPs.[29] Brownian motion can be described by the Stokes–Einstein equation[30]

$$D_{diffusion} = \frac{k_B T}{3\pi\eta d} \tag{14}$$

where $D_{diffusion}$ is the diffusion coefficient, k_B is the Boltzmann constant, T is the absolute temperature, η is the fluid viscosity, and d is the individual MNP diameter. The dipole force among MNPs has the following relation to their separation distance

$$F_{dip_{ij}} = \frac{3\mu m_i m_j}{4\pi r_{ij}^4} (r_{ij}(m_i \cdot m_j) + m_i(r_{ij} \cdot m_j) + m_j(r_{ij} \cdot m_i)$$
$$- 5 r_{ij}(r_{ij} \cdot m_i)(r_{ij} \cdot m_j)) \tag{15}$$

where i and j denote the ith and jth MNP, respectively. μ is the magnetic permeability, r_{ij} is the MNP separation distance, and m is the magnetic moment. Because Brownian motion is inversely proportional to fluid viscosity, MNPs diffuse more rapidly at low compared to high viscosities (Equation (14)), thereby promoting MNP aggregation at high viscosities (because the dipole force rapidly decreases with increasing separation distance) (Equation (15)). Consequently, the radial aggregation area is only dependent on fluid viscosity at sufficient magnetic particle concentrations. Furthermore, the radial aggregation area A_{radial} converges because the number of MNPs is finite. We propose the following curve-fitting model

$$A_{radial} = c_1 \ln(\eta) + c_2 \tag{16}$$

Herein, c_1 and c_2 are determined by comparison with experimental data (Table S1, Supporting Information). In Figure 2g, the red dot represents the calculated radial aggregation area A_{radial} based on the experimental v_{axial} (Equation (13)), and the curve fit represents the radial aggregation area A_{radial} calculated by Equation (16). The curve fit is acceptably similar (<3%) to the experimental result. The aggregation volume is a function of fluid viscosity, flow velocity, and magnetic field strength

$$V_{mmc} = f(\eta, v_f, B_{ext}) \tag{17}$$

Among the input parameters of function f, fluid viscosity and flow velocity are dependent on the surrounding environment and not controlled by the user; hence, the aggregation volume is mainly controlled by the magnetic field strength.

3.3. Verification of the Aggregation Volume Estimator

The aggregation volume estimator has calibration and real-time phases (Figure 1c). In the calibration phase, c_1 and c_2 are determined (Table S1, Supporting Information) as in Figure 2g. In the real-time phase, A_{radial} is continuously estimated based on Equation (16), and L_{axial} is estimated based on Equation (9). Based on these calculations, SMMC volume was calculated at 30 Hz (Equation (10)). To verify the aggregation volume estimator, an in vitro system was used (Figure S1b, Supporting Information). Movement of a swarm of multilayer magnetic chains was captured under a microscope (SMTUSCOPE; Shenzhen Qi Yao Technology Co., Ltd.) and the average time (t_{reach}) for a swarm of multilayer magnetic chains to migrate from the lower to the upper wall was analyzed using ImageJ (NIH) (Figure 2h). Particularly, the magnetic force and hydrodynamic drag force are related to the average time (t_{reach}). If the applied magnetic force and hydrodynamic drag force were equivalent at the MDT simulator and in vitro system, the resultant aggregation volumes in the MDT simulator and in vitro system are comparable. Herein, we compared the average time (t_{reach}) under the following conditions

Viscosity (η): 1.005, 1.769, 2.5, or 3.75 cP
Flow velocity: 2, 3, or 4 mm s^{-1}
Magnetic field at the center of the region of interest: 33 mT (1.5 A) and 45 mT (2 A)

The results, which are displayed in Figure 2i, were accurate to within an error of $t_{reach} < 10\%$. It follows that the aggregation volume estimator clearly offers accurate predictions of an aggregation volume within a 5% error.

3.4. Guidance Margin

SMMCs accelerated by a magnetic force quickly reach constant velocity due to hydrodynamic drag. We defined this constant velocity as terminal velocity. The net force applied to SMMC can be represented as

$$\sum F = -3\pi\eta d_e (v_T - v_f) + \frac{3 V_{mmc}}{\mu_0}\left(\frac{\mu - \mu_0}{\mu + 2\mu_0}\right)(B_{ext} \cdot \nabla) B_{ext} \quad (18)$$

The net force becomes zero by balancing the hydrodynamic drag forces and magnetic forces. The terminal velocity can be represented as

$$v_T = \underbrace{\frac{\overbrace{\frac{3 V_{mmc}}{\mu_0}\left(\frac{\mu - \mu_0}{\mu + 2\mu_0}\right)(B_{ext} \cdot \nabla) B_{ext}}^{\text{magnetic force effect}}}{\underbrace{3\pi\eta d_e}_{\text{viscosity effect}}}}_{} + \underbrace{v_f}_{\text{flow effect}}$$

where v_T is SMMC terminal velocity, v_f is the flow velocity, and d_e is SMMC diameter. v_T is composed of three directions: $\hat{i}$, $\hat{j}$, $\hat{k}$

(**Figure 3**a, absolute coordinates system). $\hat{i}$ is not controlled by the magnetic force but SMMCs move in that direction due to fluidic flow. The other two directions ($\hat{j}$ and $\hat{k}$) are controlled by the magnetic force. Gravitational force is ignored because it is overcome by the magnetic force at applied magnetic fields > 7 mT. SMMC trajectory is determined by the integral of v_T. The major determinants of SMMC terminal velocity (Equation (19)) are the magnetic force effect ($e_{magnetic}$), viscosity effect ($e_{viscosity}$), and flow rate (v_f)

$$
\begin{aligned}
v_T &= \frac{e_{magnetic}}{e_{viscosity}}\hat{j} + \frac{e_{magnetic}}{e_{viscosity}}\hat{k} + (\vec{v}_f \cdot \hat{i})\hat{i} + (\vec{v}_f \cdot \hat{j})\hat{j} + (\vec{v}_f \cdot \hat{k})\hat{k} \\
&= (\vec{v}_f \cdot \hat{i})\hat{i} + (\vec{v}_c \cdot \hat{j} + \vec{v}_f \cdot \hat{j})\hat{j} + (\vec{v}_c \cdot \hat{k} + \vec{v}_f \cdot \hat{k})\hat{k}
\end{aligned}
\quad (20)
$$

$e_{magnetic}$ can be controlled by the user by adjusting the magnetic field, whereas $e_{viscosity}$ and v_f are determined by the flow environment. Although the magnetic force is set as a constant, reduction of viscosity increases the terminal velocity (Equation (19)). Thus, $e_{magnetic}/e_{viscosity}$ can be represented by a single term in Equation (20) denoted as v_c. Determination of the guidance ratio and the critical guidance ratio is described in Figure 3. Both velocity vectors are time dependent: $\vec{v}_c(t)$ (yellow arrow) and $\vec{v}_f(t)$ (blue arrow). We assumed that the magnetic field was always applied toward the target entrance during MDT ($\widehat{v}_c \cdot \widehat{n}_t > 0$). $\widehat{v}_c$ is the unit vector of $\vec{v}_c(t)$ (yellow arrow) and $\widehat{n}_t$ is the direction vector of the target entrance surface (brown arrow). Among the flow velocity components ($\vec{v}_f(t)$), some are parallel to $\vec{v}_c(t)$ and contribute to SMMC guidance. This vector can be represented by calculating the dot products of $\widehat{v}_c(t)$ and $\vec{v}_f(t)$: $(\vec{v}_f(t) \cdot \widehat{v}_c)\widehat{v}_c$.

The net contribution of the velocity vector to SMMC guidance is represented as $\vec{v}_c(t) + (\vec{v}_f(t) \cdot \widehat{v}_c)\widehat{v}_c$ (black arrow), while the net non-contribution of the velocity vector to SMMC guidance is represented as $\vec{v}_f(t) - (\vec{v}_f(t) \cdot \widehat{v}_c)\widehat{v}_c$ (green arrow). Consequently, the SMMC moves in the direction of the gray arrow (sum of all vectors: $\vec{v}_c(t) + \vec{v}_f(t)$). At a magnitude of $\vec{v}_c(t)$ compared to that of $\vec{v}_f(t)$, the contact point (empty black circle) where the sum velocity vector meets the target entrance surface can be identified. By adjusting the magnitude of $\vec{v}_c(t)$, the contact line can be defined as a set of contact points (sky blue). There are two intersection points where the contact line meets the contour of the target entrance (yellow and white circles). The point at which $|\vec{v}_c(t)|$ is smallest is defined as the point of critical guidance ratio (white circle). Specifically, the white point is the minimum point of the contact line of the smallest $|\vec{v}_c(t)|$, and the yellow point is the maximum point of the contact line where $|\vec{v}_c(t)|$ is largest. When the smaller value of $|\vec{v}_c(t)|$ is used when comparing with $|\vec{v}_c(t)|$ at the point of denoted by the white circle, the SMMC cannot enter the target area. The bigger $|\vec{v}_c(t)|$ is used when comparing with $|\vec{v}_c(t)|$ at the point of denoted by the yellow circle, and SMMC can still enter the target area. For instance (Figure 3b), as $|\vec{v}_c(t)|$ decreases, SMMC guidance is hampered. By contrast, an increased $|\vec{v}_c(t)|$ value enables SMMCs to reach the vessel wall before the target entrance, and SMMCs maintain contact with the vessel wall and access the target branch due to the magnetic force rather than the flow velocity. Changes of $|\vec{v}_f(t)|$ have opposite effects on SMMC trajectory (Figure 3c, gray arrow). Changes of $|\vec{v}_c(t)|$ or $|\vec{v}_f(t)|$ shift in
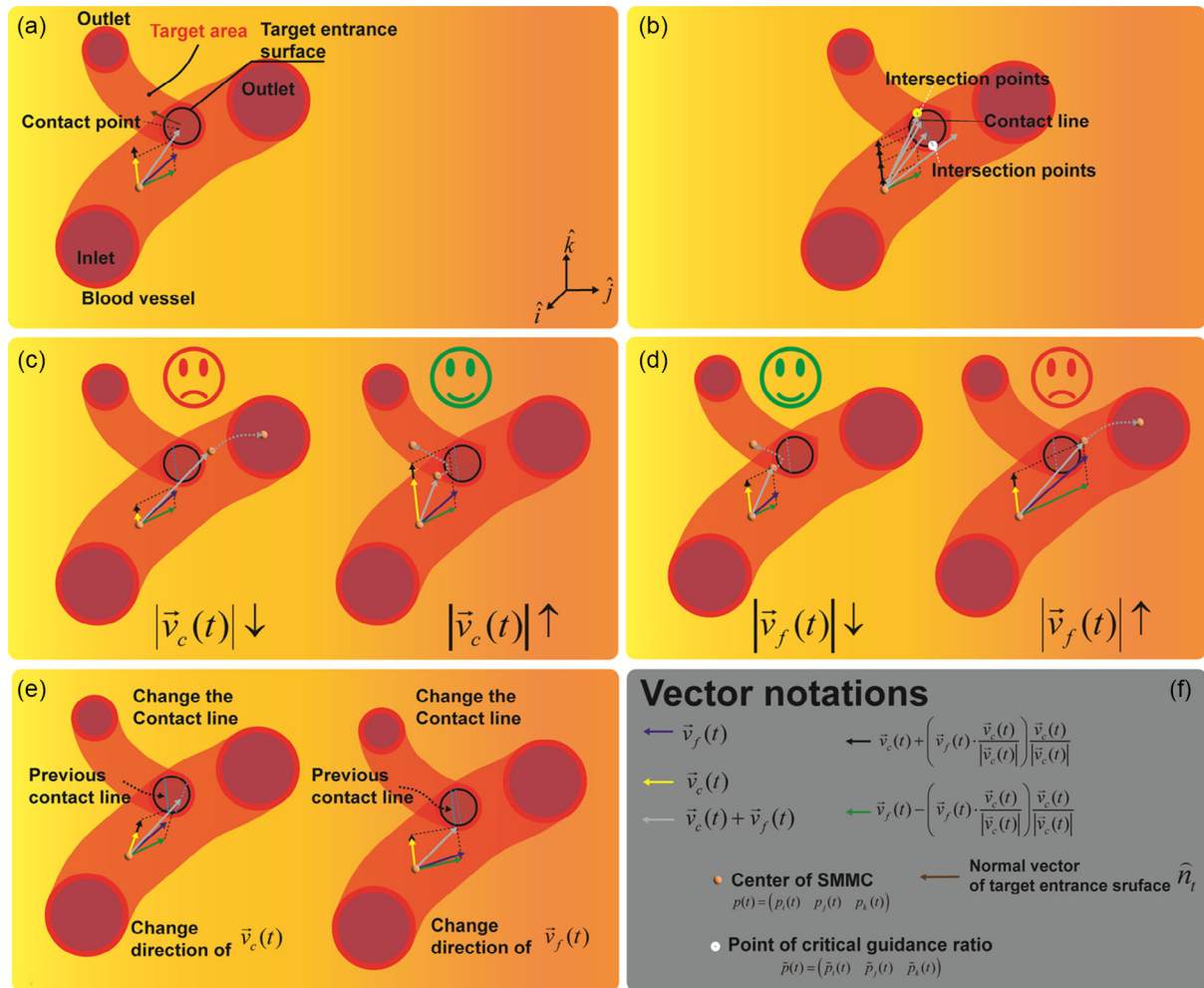
Figure 3. Determination of the guidance ratio and critical guidance ratio. a) Free diagram of the SMMC inside the blood vessel. b) The definition of the contact line and intersection points. c,d) Effects of $|\vec{v}_c(t)|$ and $|\vec{v}_f(t)|$ on SMMC trajectory. Changes of magnitude determine whether SMMC can be guided into target area or not; however, it does not affect the position of the contact line. e) By contrast, changes in the $\vec{v}_c(t)$ and $\vec{v}_f(t)$ directions alter the position of the contact line. The changes the position of the contact line lead to changes position of critical guidance ratio; hence, it will affect to critical guidance ratio. f) All vector notations are described.

the contact point but not the contact line or critical guidance ratio point. A change in direction of $\vec{v}_c(t)$ or $\vec{v}_f(t)$ shifts the contact point and contact line, thereby altering the critical guidance ratio point (Figure 3d)

The vector sum of $\vec{v}_c(t) + (\vec{v}_f(t) \cdot \widehat{v}_c)\widehat{v}_c$ and $\vec{v}_f(t) - (\vec{v}_f(t) \cdot \widehat{v}_c)\widehat{v}_c$ determines the SMMC trajectory (gray arrow). The SMMC direction is determined by the ratio of these two vectors, which in turn determines whether SMMCs are guided to the target area. Herein, we define this ratio as the guidance ratio (G_{SMMC})

$$G_{SMMC}(t) = \frac{|\vec{v}_c(t) + (\vec{v}_f(t) \cdot \widehat{v}_c)\widehat{v}_c|}{|\vec{v}_f(t) - (\vec{v}_f(t) \cdot \widehat{v}_c)\widehat{v}_c|} \tag{21}$$

The v_c term is related to fluid viscosity, magnetic field strength, magnetic field gradient, and aggregation volume; the v_f term is related to flow velocity. Thus, the guidance ratio (G_{SMMC}) is a function of the fluid viscosity, flow velocity, magnetic field strength, magnetic field gradient, and aggregation volume.

$$G_{SMMC} = g(\eta, v_f, B_{ext}, \nabla B_{ext}, V_{mmc}, t) \tag{22}$$

Among the input parameters of function g, fluid viscosity and flow velocity are determined by the environment rather than the user. Furthermore, as described in Equation (17), the aggregation volume is mainly controlled by the magnetic field strength. Therefore, the G_{SMMC} can be adjusted by modulating the magnetic field strength and gradient. The GR represents magnetic effects relative to viscous and flow-velocity effects, and so is directly related to SMMC guidance. A low guidance ratio means that the magnetic effect is insufficient, which hampers SMMC guidance. Using the critical guidance ratio point, we can determine the boundary of G_{SMMC} for SMMC guidance. The guidance ratio at the critical-guidance-ratio point is the threshold for success or failure of SMMC guidance; we denote this threshold value as the

**ADVANCED
SCIENCE NEWS**

www.advancedsciencenews.com

**ADVANCED
INTELLIGENT
SYSTEMS**
Open Access

www.advintellsyst.com

critical guidance ratio (G^*_{SMMC}), which is dependent on the position of the target area relative to the SMMC. Hence, the G^*_{SMMC} can be described as

$$G^*_{SMMC}(t) = \frac{(\widetilde{p}(t) - p(t)) \cdot \left(\frac{\vec{v}_c(t) + (\vec{v}_f(t) \cdot \vec{v}_c)\widehat{\vec{v}}_c}{|\vec{v}_c(t) + (\vec{v}_f(t) \cdot \vec{v}_c)\widehat{\vec{v}}_c|}\right)}{(\widetilde{p}(t) - p(t)) \cdot \left(\frac{\vec{v}_f(t) - (\vec{v}_f(t) \cdot \vec{v}_c)\widehat{\vec{v}}_c}{|\vec{v}_f(t) - (\vec{v}_f(t) \cdot \vec{v}_c)\widehat{\vec{v}}_c|}\right)} \quad (23)$$

where the critical-guidance-ratio point is $\widetilde{p}(t)$ and the SMMC center position is $p(t)$.

The guidance margin can be calculated during simulation time T using the guidance ratio and the critical guidance ratio. The guidance margin conditions are as follows

$$\begin{bmatrix} G_{margin} = \frac{1}{T}\int_0^T (G_{SMMC} - G^*_{SMMC})dt \\ G_{margin} > 0 \text{ controllable} \\ G_{margin} \leq 0 \text{ uncontrollable} \end{bmatrix} \quad (24)$$

where G_{margin} is the guidance margin (**Table 1**). If the guidance margin is positive, the SMMC can be guided to the target area (controllable). When the guidance margin is negative, the SMMC cannot be guided to the target area (uncontrollable).

4. Results

4.1. Rat-Brain Vessel Model

We focused on the rat-brain ICA, MCA, and ACA. The ICA is a major branch of the common carotid artery and supplies blood to several parts of the head. Occlusion of the ICA, MCA, and ACA can cause stroke, leading to significant morbidity and mortality.[31] MNP guidance in the ICA–MCA–ACA pathway would enable minimally invasive treatment. The experimental conditions were as follows:
Fluids: glycerol mixture, blood
Viscosities (η): 1.75, 3.75, and 5.75 cP
Flow velocities: 1, 2, and 5 mm s^{-1}
Targets: default, MCA, ACA, ACA2

Table 1. Guidance margins.

Fluid[a]	Mode	1 mm s^{-1}	2 mm s^{-1}	5 mm s^{-1}
Glycerol mixture (1.75 cP)	MCA	0.85 (○)	0.14 (○)	−0.138 (×)
	ACA	0.301 (○)	0.0525 (○)	−0.0478 (×)
	ACA2	0.139 (○)	0.008 (○)	−0.0321 (×)
Glycerol mixture (3.75 cP)	MCA	0.416 (○)	0.021 (○)	−0.172 (×)
	ACA	0.143 (○)	0.0135 (○)	−0.0585 (×)
	ACA2	0.065 (○)	0.00195 (○)	−0.0384 (×)
Glycerol mixture (5.75 cP)	MCA	0.206 (○)	−0.052 (×)	−0.187 (×)
	ACA	0.0465 (○)	−0.0265 (×)	−0.0615 (×)
	ACA2	0.055 (○)	−0.014 (×)	−0.0405 (×)
Blood	MCA	0.364 (○)	−0.007 (×)	−0.184 (×)
	ACA	0.1 (○)	−0.0035 (×)	−0.0605 (×)
	ACA2	0.08 (○)	−0.009 (×)	−0.0391 (×)

[a]Symbols indicate guidance margins in the controllable (○) and uncontrollable (×) ranges.

4.2. Guidance in the Simulation and In Vitro

4.2.1. Trajectory Generation in the MDT Simulator

In the MDT simulator, the user guided the SMMC center point to the target area; representative center points of the SMMC trajectories are shown in Figure S4, Supporting Information. The guidance ratio and critical guidance ratio are affected by flow velocity and fluid viscosity, as is the guidance margin (calculated by Equation (24); Table 1).

4.2.2. Guidance in Simulation Testbed

In the simulation, 600 MNPs were used to verify the aggregation model–based OLPG at various fluid viscosities and flow velocities (Figure S5, Supporting Information). Under a magnetic field, some MNPs aggregated (aggregated MNPs), whereas others remained suspended (isolated MNPs). The proportion of suspended MNPs was affected by their concentration, magnetic field strength, flow velocity, and fluid viscosities.[29] We determined the percentage of suspended MNPs based on the Y-channel (Figure S6a, Supporting Information). In the absence of a magnetic field, MNPs were distributed throughout the channel (Figure S6b, Supporting Information). Once a magnetic field is applied toward the right, aggregated MNPs are guided to the right side, and non-aggregated MNPs are distributed throughout the channel (Figure S6c, Supporting Information). After the end of experiment, we checked the particle concentration of each outlet using a particle concentration device (Varioskan LUX Multimodal Microplate Reader). We calculated the percentage of suspended MNPs (Table S2, Supporting Information) by comparison with the default mode (Figure S6b, Supporting Information). We defined the volume range of suspended MNPs as 2.244×10^{-20} to 4.48921×10^{-19} m^3, as calculated by the Brownian motion equation (Note S1, Supporting Information). The motion of suspended MNPs was predominantly determined by Brownian motion.

When the SMMC trajectory was generated by the MDT simulator (Figure S4, Supporting Information), SMMC volume was continuously estimated using the aggregation volume estimator. In the simulation, the minimum and maximum volumes are set as the boundaries of the aggregated particle volume (Figure S7, Supporting Information), enabling the aggregated magnetic particles to be of inconstant volume due to the randomness of aggregation.[28]

MNP guidance is affected by viscosity and flow velocity (**Figure 4**a). In default mode, 19.34% of MNPs reached the ACA and 80.67% reached the ACA2. MNP trajectory was dependent on the initial injection position. We injected MNPs using a microsyringe (NanoFil 34-gauge; inner diameter = 0.051 mm) near the center of the inlet and far from the MCA branch. Therefore, many MNPs are guided to the ACA and ACA2 in default mode.

In MCA mode (1.75 cP and 1 mm s^{-1}), 69.07% of MNPs were guided to the MCA, 5.8% to the ACA, and 25.13% to the ACA2. However, suspended MNPs were present in the ACA and ACA2. Therefore, although the SMMC center position was guided to the target area, the targeting performance was <100%. In ACA mode (1.75 cP and 1 mm s^{-1}), MNPs were detected only in the ACA
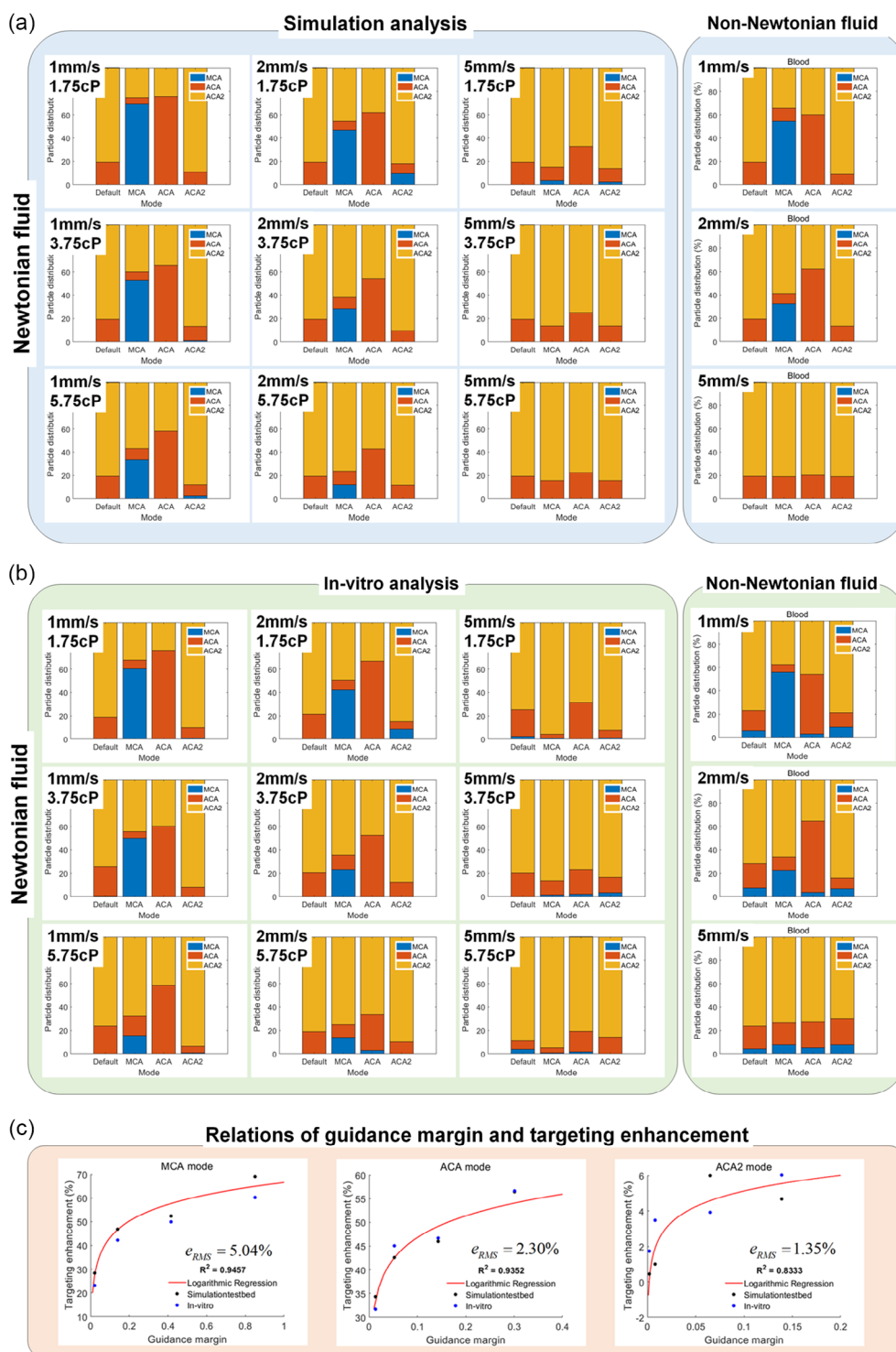
Figure 4. a) Targeting performance in a simulation testbed and b) in vitro analysis according to viscosity, flow velocity, and fluid. c) Relationship of guidance margin with targeting enhancement compared with the default mode.

and ACA2, and 75.8% were guided to the ACA. In ACA2 mode (1.75 cP and 1 mm s^{-1}), 89.3% of MNPs were guided to the target area. The presence of two branches prior to the ACA2 complicates guidance. Furthermore, MNPs reached the ACA2 in the

absence of a magnetic force. Consequently, targeting performance is slightly improved compared with the default mode.

An increase of flow velocity (2 mm s^{-1}) reduced the effect of magnetic force on MNP trajectory (Equation (19)), increased the

**ADVANCED
SCIENCE NEWS**

www.advancedsciencenews.com

**ADVANCED
INTELLIGENT
SYSTEMS**
Open Access

www.advintellsyst.com

percentage of suspended MNPs (Table S2, Supporting Information), and reduced the amount of aggregated MNPs guided to the target area. At a higher flow velocity (5 mm s^{-1}), the aggregated MNPs follow fluidic flow, thereby reducing the amount guided to the target area (Figure 4a). Increases in viscosity (Equation (19)) had similar effects (Figure 4a).

In blood (Figure 4a), in default mode, MNPs followed fluidic flow due to the absence of an external magnetic field so that the particles have the same distribution as Newtonian fluids. Targeting performance in blood decreased with increasing flow velocity. At a flow velocity of 1 mm s^{-1}, targeting performance is similar to that at a viscosity of 3.75 cP because the viscosity of MNPs in blood is 3–5 cP (near vessel walls). At a flow velocity of 2 mm s^{-1}, targeting performance was improved compared to a Newtonian fluid (3.75 cP). In blood, an increase in flow velocity decreases viscosity (Figure S8, Supporting Information), thereby improving targeting performance (≈5%). At a flow velocity of 5 mm s^{-1}, there was no significant difference between a Newtonian fluid (glycerol mixture) and non-Newtonian fluid (blood).

4.2.3. Guidance In Vitro

We evaluated the aggregation model–based OLPG scheme in vitro (Figure S9, Supporting Information) using a particle concentration analyzer (Varioskan LUX Multimodal Microplate Reader) (Figure 4b). To visualize MNP distributions, we performed fluorescence imaging (IVIS Lumina; Xenogen) at 1 mm s^{-1} and 3.75 cP and compared the data with that obtained from the simulation (**Figure 5**a,b). Targeting performance in vitro was comparable to the simulation (Figure 4a,b). In default mode, MNPs reached the ACA and ACA2, and some reached the MCA. The MNP distributions differed slightly between the simulation and in vitro analysis because Brownian motion was not accounted for in the simulation (Note S1, Supporting Information).

In MCA mode, fewer MNPs were guided to the target area compared with the simulation (Figure 4a,b). Many MNPs passed through the MCA branch in MCA mode, but some remained at the entrance to the MCA due to their diffusion properties (Figure 5a,b).[32] The remaining MNPs exited via the ACA or ACA2 due to fluidic flow. Thus, compared with the simulation, more MNPs reached the ACA or ACA2 than the MCA. In ACA mode, targeting performance in the simulation was similar to that in vitro (Figure 4a,b). Many MNPs passed through the ACA branch (Figure 5a,b). Although some MNPs did not reach the ACA, they reached the ACA or ACA2 due to fluidic flow. In ACA2 mode (Figure 4a,b), targeting performance was similar to that in the simulation: MNPs reached the ACA2 and ACA (Figure 5a,b). In blood (Figure 4a,b), the MNP distribution at the in vitro experiment was slightly different from that in the simulation due to Brownian motion and disturbances by RBCs (<5%).

4.2.4. Guidance Margin

Comparison of the guidance margin (Table 1) between the simulation (Figure 4a) and in vitro data (Figure 4b) indicated a logarithmic regression relation (Figure 4c) with enhancement of targeting performance. The positive guidance margin data are shown because SMMCs cannot be guided to a target area if the guidance margin is negative.

The logarithmic regression is modeled using the guidance margin calculated in the MDT simulator (red line) and enhanced targeting performance in the simulation (black dot) (Figure 4c). The coefficients of determination (R^2) were 0.9457, 0.9352, and 0.8333 for the MCA, ACA, and ACA2, respectively. The differences between the modeled and simulated results were caused by the percentage of isolated particles and unaccounted-for forces. In ACA2 mode, little external control is needed to guide MNPs to the target area because they tend to move toward the target area because of the injection position; MNP trajectory is
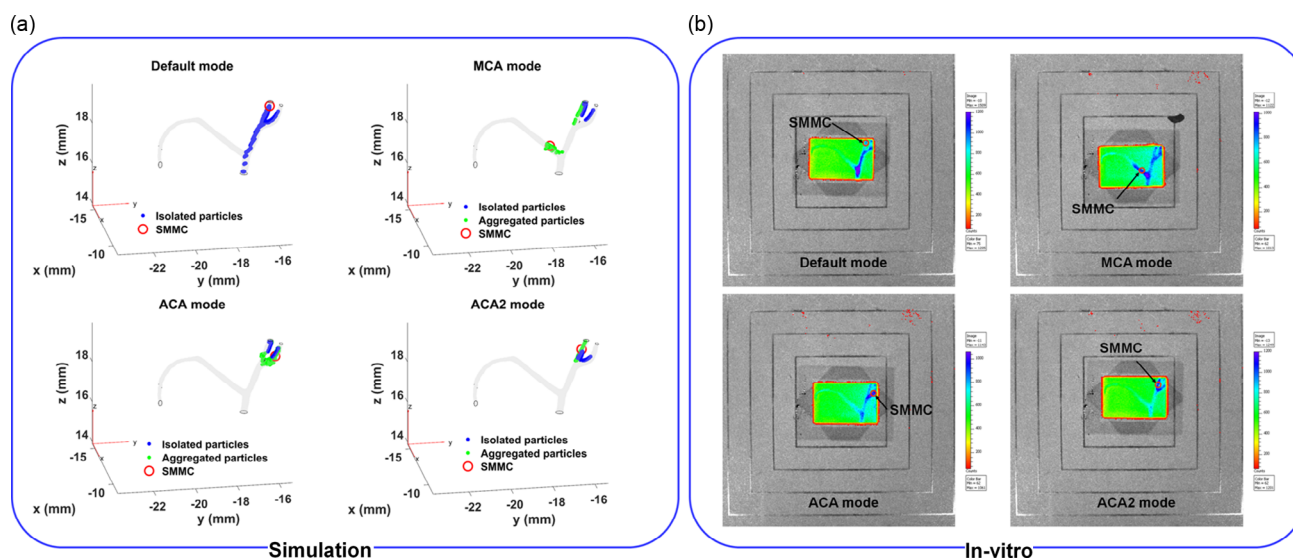

Figure 5. a) Magnetic nanoparticles (MNP) distributions in the simulation and b) in vitro at 3.75 cP and 1 mm s^{-1}. The particle distribution and SMMC position are compared.

**ADVANCED
SCIENCE NEWS**

www.advancedsciencenews.com

**ADVANCED
INTELLIGENT
SYSTEMS**
Open Access

www.advintellsyst.com

affected by Brownian motion, electrostatic forces, and Van der Waals forces.[29] As a result, the relationship between the guidance margin and enhanced targeting performance is weak. The differences between the simulation (Figure 4a) and in vitro (Figure 4b) data are caused by aggregation modeling errors, RBCs, unaccounted-for forces, and the nonuniform sizes of MNPs. The root-mean-square error (Figure 4c) in all modes was <5.04%, indicating that the logarithmic regression model accurately reflects the in vitro results.

4.2.5. Verification of the Aggregation Volume Estimator

The OLPG was verified by simulation and in vitro analysis. We compared the OLPG with and without the aggregation volume estimator (**Figure 6**). In the absence of the aggregation volume estimator, SMMC volume was determined at the initial state and remained constant during guidance to the target area (Figure 6a). By contrast, in the presence of the aggregation volume estimator, SMMC volume was estimated continuously during guidance (Figure 6b). The simulation used blood at a flow velocity of 2 mm s^{-1}. The SMMC center point and aggregated MNP trajectories, SMMC volume, and applied current intensity are shown in Figure 6a,b. The trajectory of isolated MNPs is excluded because they are not controllable.

As shown in Figure 6a, the SMMC center point represents the aggregated MNPs. Without the aggregation volume estimator, the difference between the positions of aggregated MNPs and the SMMC center point was greater, which hampered guidance of MNPs to the target area. SMMC volume is shown in Figure 6a, b. The fluid viscosity and flow velocity vary positionally, thereby altering SMMC volume. Moreover, changes in magnetic field strength affect SMMC volume with the aggregation volume estimator (Figure S10, Supporting Information). The targeting performance is shown in Table 1. Targeting performance was improved by the aggregation volume estimator both in the simulation and in vitro. OLPG without the aggregation volume estimator in blood (2 mm s^{-1}) improved targeting performance by 106%–175% compared to default mode, whereas OLPG with

the aggregation volume estimator improved targeting performance by 116%–409%. The aggregation volume estimator improved targeting performance by 111%–180% compared to OLPG without the aggregation volume estimator (**Table 2**).

4.2.6. Pulsatile Flow

In this section, we validated the proposed guidance scheme under the pulsatile flow environment through the studies in the simulation testbed. The inlet average blood flow velocity was modeled using sinusoidal function as $v_f = A(\sin(2\pi ft + \pi/6) + 1)$.[33] Where input flow velocity frequency f is set as 1, t is the time and the amplitude A is set as 2 due to the limitation of our current system (magnetic field is limited) (**Figure 7**a). A total of 100 particles are used for the simulation. A total of 50 particles have the properties of isolated particles, while 50 particles have the properties of aggregated particles. We can observe that the aggregated particles (Figure 7c,f) follow the SMMC trajectory (Figure 7b). The trends of guidance results in pulsatile flow are comparable with the guidance results in the steady flow. Furthermore, from the guidance margin value, we can estimate the targeting enhancement through the regression model (Figure 4). Compared to the estimated targeting enhancement and the target enhancement in the simulation testbed, it is obvious that predicting the targeting enhancement using guidance margin is still valid when the pulsatile flow is injected instead of the steady flow (error < 3.88%) (**Table 3**).

5. Discussion

We investigated the relationships among magnetic field strength, fluid viscosity, flow velocity, and aggregation volume by mathematical modeling and in vitro. On the basis of the investigation, an analytic model for calculating aggregation volume was suggested and an aggregation volume estimator was developed. Also, we developed an OLPG scheme with an aggregation volume estimator. We validated the proposed guidance scheme using 3D phantoms under varying conditions. The simulation
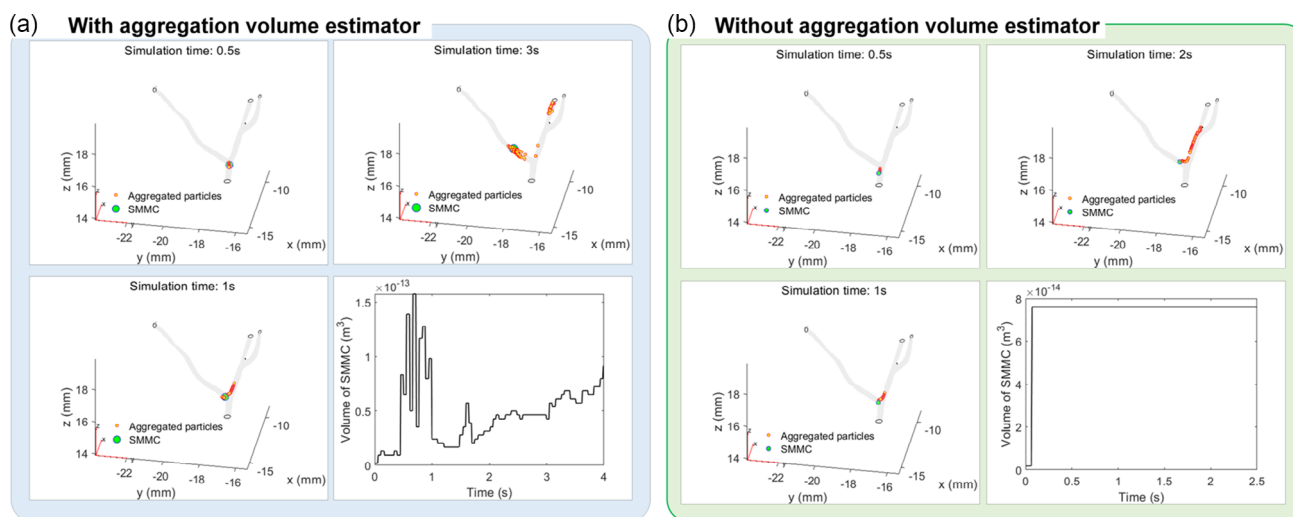

Figure 6. OLPG results a) with and b) without the aggregation volume estimator in MCA mode (blood and 2 mm s^{-1}).

Table 2. Targeting performance with and without the aggregation volume estimator.

| 2 mm s^{-1} blood	MCA [%]	ACA [%]	ACA2 [%]	2 mm s^{-1} blood	MCA [%]	ACA [%]	ACA2 [%]
Target	Simulation—without aggregation volume estimator			Target	In vitro—without aggregation volume estimator		
Default	0	19.34	80.67	Default	9.65	19.83	70.52
MCA	6.14	12.56	81.3	MCA	16.94	15	68.06
ACA	0	35.5	64.5	ACA	3.6	47.32	49.08
ACA2	0	20.17	79.83	ACA2	4.5	20.15	75.35
Target	Simulation—with aggregation volume estimator			Target	In vitro—with aggregation volume estimator		
Default	0	19.34	80.67	Default	7.47	20.56	71.97
MCA	32.3	8.99	59.71	MCA	30.56	11.47	61.97
ACA	0	62.13	37.87	ACA	3.63	60.97	35.4
ACA2	0	13.4	86.6	ACA2	6.69	9.38	83.93
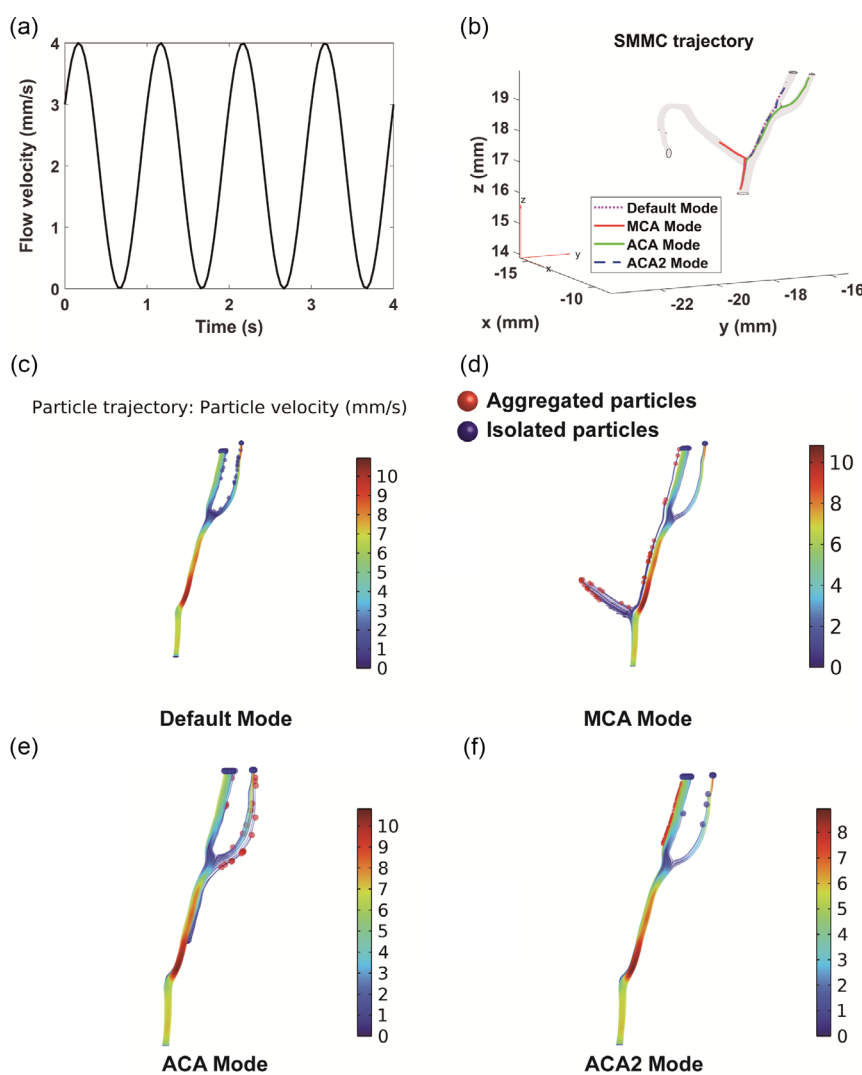
Figure 7. Guidance results in the simulation testbed. a) Pulsatile flow injection, b) SMMC trajectory, particle trajectories, and distribution at c) the default mode, d) MCA mode, e) ACA mode, and f) ACA2 mode.

and in vitro results showed that MNPs can be guided to target areas with no need for imaging.

Our method enables the guidance of MNPs to target areas in rat-brain blood vessels. Although microswarm techniques were

**ADVANCED
SCIENCE NEWS**

www.advancedsciencenews.com

**ADVANCED
INTELLIGENT
SYSTEMS**

Open Access

www.advintellsyst.com

Table 3. Results of particle distribution under the pulsatile flow.

Mode	Guidance margin	Estimated targeting enhancement	Target			Targeting enhancement in simulation testbed
			MCA	ACA	ACA2	
Default			0	16	84	
MCA	0.941×10^{-3}	35.88	32	60	8	32
ACA	0.229×10^{-3}	37.98	0	52	48	36
ACA2	0.061	6.51	0	8	92	8

suggested for MDT,[34] maintaining MNP swarms under the fluidic flow is challenging[35] and hampered by the lack of 3D locomotion schemes.[36] In vivo imaging of micro/nanorobot swarms is still in its infancy.[37,38] MDT tasks which involve 3D bloodstreams should be verified further. Under the fluidic flow, the swarm formation or aggregation of MNPs is affected by the surrounding flow environment; hence, the existing guidance schemes for a swarm may not be valid without tracking aggregation changes or maintaining a swarm formation. In this regard, the aggregation volume estimator was proposed to estimate aggregation changes. The development of an aggregation volume estimator realizes that the aggregation volume is calculated in real time using information on the surrounding blood vessels and guarantees the validity of the guidance scheme for MNPs to the target area with high targeting performances. A magnetic field gradient is used to have 3D locomotion of the MNPs and their motion is not confined to the surface-walker motion.[39] OLP concepts can be an alternative guidance scheme without the need of real-time in vivo imaging.[40] Moreover, we introduced the guidance margin, which is calculated from the magnetic field, magnetic field gradient, aggregation volume, and MNP properties. Although magnetic field strength, magnetic field gradient, and MNP properties can be mathematically modeled or measured, modeling of aggregation volume is not possible. The development of the aggregation volume estimator enables the estimation of aggregation volume and draws out the introduction of the guidance margin. By comparing the targeting enhancement in the simulation and in vitro results with the guidance margin, we could identify the correlation between the guidance margin and targeting enhancement. MNPs were guided to target areas via blood at flow velocities of 1 and 2 mm s^{-1} and viscosities of 1.75, 3.75, and 5.75 cP. The use of an aggregation volume estimator improved targeting performance.

Our demonstration indicates that the proposed guidance scheme is feasible to navigate MNPs into the target area up to the flow velocity of 2 mm s^{-1}, as per proper guidance scheme in the capillaries.[41] Although the proposed guidance scheme is effective in a variety of flow environments, it fails at flow velocities >5 mm s^{-1} due to limitation of magnetic force. Higher magnetic force can provide the chance to guide MNPs into the target area such as Aorta, Artery, and Arteriole which are in high flow velocities. The construction of a coil system[42] or increasing particle susceptibility[43] can help to generate a high magnetic field gradient. In an alternative way, the blood flow velocity can be temporarily reduced nearby the target area using

vascular clamps,[44] this can help to manipulate MNPs against the flow velocities. The locomotion nearby vessel boundary is one of the prominent ways to overcome the drastic blood flow.[17] The velocity of blood flow is dramatically reduced near the walls due to properties of laminar flow and nonslip boundary conditions. Recently, surface-induced locomotion "surface-walker" was introduced.[39] Meanwhile, the proposed offline programming guidance scheme is not restricted to the guidance scheme using the magnetic field gradient but it can be extended to the other guidance scheme using other external power-driven sources.[45–47] For instance, by modeling the surface-induced locomotion mathematically,[48] the MDT simulator can be implemented and resultant offline programming guidance scheme for "surface-walker" can be developed. When using different types of external field, such as oscillating or rotating fields, the formation of aggregation will change. The shape of aggregation significantly affects the hydrodynamic drag force.[49] For instance, we analyzed the effects of aggregation shape when magnetic force was applied (Note S4, Supporting Information). The aggregation shape affects the terminal velocity of the aggregate and can, therefore, affect the targeting performance. Consequently, the aggregation shape model has to be determined according to the external field.

Furthermore, the used realistic vessel model is obtained from the UTE–MRA image of a rat brain; hence, we can say this model mimics the real structure of the brain vessel but does not the intravascular conditions. The MNPs have interactions with bio-components[50] not only with RBCs at the intravascular conditions. Furthermore, the interaction between MNPs and vessel walls may affect on the targeting performance significantly.[51] The consideration of the interaction forces with the bio-components and wall conditions makes our system more precise. However, there is trade-off between the precision of the simulation and time consumption; hence, the real-time MDT simulator cannot be established with consideration of all interaction forces. In this article, the proposed guidance scheme was well operated under the blood conditions (targeting results are reduced by around ≈5% compared with the simulation results). These results show that the current MDT simulator is acceptable in agreement with in vitro environment and it has potential to implement targeted drug delivery under the vivo environment with simplifying intravascular conditions.

6. Conclusion

We developed an aggregation volume estimator–based OLPG method. To calibrate the MDT simulator, an aggregation volume estimator model was developed and validated in vitro. The method enabled guidance of MNPs to a target area via the bloodstream at a flow velocity of 1–2 mm s^{-1}. The simulation and in vitro results were in acceptable agreement. The guidance method has considerable potential for biomedical applications. The guidance margin was dependent on the viscosity, magnetic force, and flow velocity. Evaluating the guidance margin enabled prediction of targeting performance, which will facilitate design of EMA systems and determination of MNP properties or guidance algorithms. In future, we plan to guide MNPs in a rat-brain blood vessel in vivo using the proposed guidance method.

7. Experimental Section

Materials: Fluorescent carboxyl magnetic Nile red particles (FMNPs; 0.2–0.39 μm diameter, 1% w/v) polymerized with styrene were purchased from Spherotech (FCM-02556-2). Transmission electron microscopy (Tecnai G2 F30 S-Twin; FEI) revealed smooth spherical nanoparticles with an average diameter of 350 μm (Figure S3a, Supporting Information). The magnetic response (magnetization curve) of the magnetic particles is shown in Figure S3b, Supporting Information. This curve was mathematically modeled using the Langevin function.[52] The applied flux density range was ±500 mT and the magnetic susceptibility of the MNPs was measured using a vibrating sample magnetometer (Lake Shore Cryotronics). Sheep whole blood (Carolina Biological Supply Company) was used. A 3D blood-vessel model was created from photopolymer resin using a 3D printer.

MNPs were collected using a permanent magnet (Figure S11, Supporting Information) and allowed to sediment in tubes for 30 min. The MNPs were separated and suspended in water (50 μL). To measure the MNP concentration, 200 μL of HCL was added and mixed. Next, 50 μL was removed, 150 μL of KSCN was added, and the plate was read at 490 nm using a microplate reader (Varioskan LUX Multimodal Microplate Reader; ThermoFisher Scientific) with Skanlt software. The results were transformed to iron concentrations to calculate particle distribution (Figure S9, Supporting Information).

Force Applied to MNPs: The total applied force on MNPs was calculated as follows

$$m_i \frac{dv_i}{dt} = F_{mf} + F_{drag} + F_{grav} + F_{wall} \tag{25}$$

Using Newtonian dynamics, a governing equation was modeled where index *a* defines particle *i*, m_i is particle mass, and v_i is particle velocity. In this equation, F_{mf} is the magnetic force, F_{drag} is the hydrodynamic drag force, F_{wall} is the interparticle interaction force, and F_{grav} is the gravitational force. F_{mf} is the actuation force used to steer particles, *m* is the magnetic moment (Equation (2)), and B_{ext} is the external magnetic field.

$$F_{mf} = (m \cdot \nabla)B_{ext} \tag{26}$$

The hydrodynamic drag force (F_{drag}) induced by flow rate v_f can be expressed by the modified Stock law with a Stokes shape correction factor, f_c, particle velocity, v_p, and effective diameter, d_e, as in ref. [26]

$$F_{drag} = 3\pi \eta d_e f_c (v_p - v_f) \tag{27}$$

The gravitational force (F_{grav}) is modeled as

$$F_{grav} = V(\rho_p - \rho_f)g \tag{28}$$

where ρ_p and ρ_f are the particles and fluid density, respectively; *V* is particle volume; and *g* is gravitational acceleration. The particle wall force, F_{wall}, was activated when particles approached the wall and could be modeled based on modified Lennard–Jones (LJ) interaction forces[48]

$$F_{wall} = \frac{\varepsilon}{h - d/2}\left[\left(\frac{\sigma}{h - d/2}\right)^{12} - \left(\frac{\sigma}{h - d/2}\right)^6\right] \tag{29}$$

where *h* is the wall–particle distance, ε is the depth of the potential well, *d* is particle diameter, and σ is the distance at which the particle–wall potential energy is zero. Laminar blood flow was expected in the brain blood–vessel model due to the small Reynolds number ($<10^{-5}$). We ignored the turbulence generated in arteries by heart pumping; this is reasonable if we consider a blood vessel far from the heart. The incompressible Navier–Stokes equations were solved for the Eulerian frame along with a model for the discrete motion of particles in a Lagrangian frame. The Carreau model was used to describe non-Newtonian fluids (blood), the viscosity of which is as follows

$$\nu = \nu_\infty + (\nu_0 - \nu_\infty)[1 + \lambda^2 \dot{\gamma}^2]^{\frac{n-1}{2}} \tag{30}$$

where $\dot{\gamma}$ is the shear rate, ν_∞ is the viscosity at infinite shear rate, ν_0 is the viscosity at zero shear rate, λ is the relaxation time, and n is the power index.[53]

Magnetic Field Modeling: We modeled a magnetic field using the off-axis equation and compared the data with measurements. The EMAs consisted of four magnetic coils on the x- and y-axes (Figure S12, Supporting Information). Each coil had an iron core to increase the magnetic field strength.[54] At any point in the system, the magnetic field is the superposition of the fields induced by each coil and can be obtained by integrating the Biot–Savart law over the circular current loop. The magnetic field *B* due to a single-current loop can be computed by evaluating the curl of the magnetic vector potential *A*. At any point in the xyz-plane (i.e., P(ρ,ϕ,z)), the magnetic vector potential A produced by a constant current I in a current loop can be calculated by

$$A(\rho, \phi, z) = \frac{\mu_0 I a}{4\pi} \int_0^{2\pi} \frac{\cos(\phi)d\phi}{\sqrt{a^2 + \rho^2 + z^2 - 2a\rho\cos(\phi)}}$$
$$= \frac{\mu_0}{\pi} \frac{Ia}{(a+\rho)^2 + z^2}\left[\frac{(2-k^2)E_2(k) - 2E_1(k)}{k^2}\right] \tag{31}$$

where *a* is the radius of the coil; ρ, ϕ, and *z* are the cylindrical coordinates; μ_0 is the permeability of air; $E_1(k)$ and $E_2(k)$ are the complete elliptic integrals of the first and second kind, respectively; and the argument *k* of the elliptic integrals is

$$k^2 = \frac{4\rho a}{(a+\rho)^2 + z^2} \tag{32}$$

Because magnetic field *B* is the curl of vector field *A*, based on the law of Biot–Savart, the components of magnetic induction in cylindrical coordinates are

$$B = \nabla \times A \tag{33}$$

$$B_\rho = -\frac{1}{\rho}\frac{\partial(\rho A)}{\partial z} = \frac{\mu_r z}{2\pi\rho\sqrt{(a+\rho)^2 + z^2}}\left(\frac{a^2 + z^2 + \rho^2}{z^2 + (\rho - a)^2}E_2(k) - E_1(k)\right)NI \tag{34}$$

$$B_z = \frac{1}{\rho}\frac{\partial(\rho A)}{\partial \rho} = \frac{\mu_r}{2\pi\sqrt{(a+\rho)^2 + z^2}}\left(\frac{a^2 - z^2 - \rho^2}{z^2 + (\rho - a)^2}E_2(k) + E_1(k)\right)NI \tag{35}$$

Unlike the single-current loop, to generate a high magnetic field with a compact device, multilayer coils with iron cores were used. The number of turns *N* was multiplied by the current *i* in the coil. To prevent high-frequency losses, the maximum frequency was 10 Hz. An iron core was inserted into each coil to enhance the magnetic field strength. The permeability of the air, μ_0, was replaced by the permeability of the core, μ_r.

In a 3D Cartesian coordinates workspace, the magnetic field of an arbitrary position, $B_{(x,y,z)}$, could be represented as the superposition of magnetic fields induced by the four coils. The applied magnetic field on magnetic particles could be calculated as follows

$$\begin{bmatrix} B_x \\ B_y \\ B_z \end{bmatrix} = \begin{bmatrix} B_{1z} - B_{2\rho}\cos\phi_2 - B_{3z} + B_{4\rho}\cos\phi_4 \\ B_{1\rho}\cos\phi_1 + B_{2z} - B_{3\rho}\cos\phi_3 - B_{4z} \\ B_{1\rho}\sin\phi_1 + B_{2\rho}\sin\phi_2 + B_{3\rho}\sin\phi_3 + B_{4\rho}\sin\phi_4 \end{bmatrix} \tag{36}$$

Supporting Information

Supporting Information is available from the Wiley Online Library or from the author.

Acknowledgements

Conflict of Interest

The authors declare no conflict of interest.

Data Availability Statement

The data that support the findings of this study are available from the corresponding author upon reasonable request.

Keywords

[1] R. Singh, J. W. Lillard Jr, *Exp. Mol. Pathol.* **2009**, *86*, 215.
[2] B. J. Nelson, I. K. Kaliakatsos, J. J. Abbott, *Annu. Rev. Biomed. Eng.* **2010**, *12*, 55.
[3] Y. Alapan, U. Bozuyuk, P. Erkoc, A. C. Karacakol, M. Sitti, *Sci. Rob.* **2020**, *5*, aba5726.
[4] F. U. Amin, A. K. Hoshiar, T. D. Do, Y. Noh, S. A. Shah, M. S. Khan, J. Yoon, M. O. Kim, *Nanoscale* **2017**, *9*, 10619.
[5] M. Grassi, G. Grassi, R. Lapasin, I. Colombo, *Understanding Drug Release and Absorption Mechanisms: A Physical and Mathematical Approach*, CRC Press, Boca Raton, Florida **2006**.
[6] A. Dash, G. Cudworth II, *J. Pharmacol. Toxicol. Methods* **1998**, *40*, 1.
[7] S. Martel, *J. Nanopart. Res.* **2015**, *17*, 1.
[8] Q. Wang, L. Zhang, *ACS Nano* **2021**, *15*, 149.
[9] Y. Chen, D. Chen, S. Liang, Y. Dai, X. Bai, B. Song, D. Zhang, H. Chen, L. Feng, *Adv. Intell. Syst.* **2022**, *4*, 2100116.
[10] D. Ahmed, A. Sukhov, D. Hauri, D. Rodrigue, G. Maranta, J. Harting, B. J. Nelson, *Nat. Mach. Intell.* **2021**, *3*, 116.
[11] Y.-L. Liu, D. Chen, P. Shang, D.-C. Yin, *J. Controlled Release* **2019**, *302*, 90.
[12] M. Hu, X. Ge, X. Chen, W. Mao, X. Qian, W.-E. Yuan, *Pharmaceutics* **2020**, *12*, 665.
[13] A. K. Hoshiar, T.-A. Le, F. U. Amin, M. O. Kim, J. Yoon, *J. Magn. Magn. Mater.* **2017**, *427*, 181.
[14] M. Park, T.-A. Le, Y. Hadadian, J. Yoon, *J. Magn. Magn. Mater.* **2022**, *564*, 170110.
[15] N. Li, Y. Jiang, R. Plantefève, F. Michaud, Z. Nosrati, C. Tremblay, K. Saatchi, U. O. Häfeli, S. Kadoury, G. Moran, *Ann. Biomed. Eng.* **2019**, *47*, 2402.
[16] P. Vartholomeos, C. Mavroidis, *IEEE Trans. Biomed. Eng.* **2012**, *59*, 3028.
[17] Q. Wang, K. F. Chan, K. Schweizer, X. Du, D. Jin, S. C. H. Yu, B. J. Nelson, L. Zhang, *Sci. Adv.* **2021**, *7*, abe5914.
[18] L. Yang, J. Yu, S. Yang, B. Wang, B. J. Nelson, L. Zhang, *IEEE Trans. Rob.* **2021**.
[19] G. Wittenberg, *Ind. Rob. Int. J.* **1995**, *22*, 21.
[20] M. Park, T.-A. Le, J. Yoon, *IEEE Rob. Autom. Lett.* **2022**, *7*, 3977.
[21] M. Luo, J. Law, X. Wang, L. Xin, G. Shan, M. Badiwala, X. Huang, Y. Sun, *2020 IEEE Int. Conf. on Robotics and Automation (ICRA)*, IEEE **2020**, pp. 4470–4476.
[22] M. Kang, S. Jin, D. Lee, H. Cho, *Sci. Rep.* **2020**, *10*, 4989.
[23] D. J. Klingenberg, J. C. Ulicny, M. A. Golden, *J. Rheol.* **2007**, *51*, 883.
[24] J. Ku, X. Liu, H. Chen, R. Deng, Q. Yan, *AIP Adv.* **2016**, *6*, 025004.
[25] V. Schaller, U. Kräling, C. Rusu, K. Petersson, J. Wipenmyr, A. Krozer, G. Wahnström, A. Sanz-Velasco, P. Enoksson, C. Johansson, *J. Appl. Phys.* **2008**, *104*, 093918.
[26] E. Loth, *Powder Technol.* **2008**, *182*, 342.
[27] A. G. Koutsiaris, *Clin. Hemorheol. Microcirc.* **2009**, *43*, 321.
[28] P. Pálovics, M. Rencz, *Microsyst. Technol.* **2022**, *28*, 1545.
[29] E. Karvelas, N. Lampropoulos, L. Benos, T. Karakasidis, I. E. Sarris, *Comput. Methods Programs Biomed.* **2021**, *198*, 105778.
[30] K. A. Dill, S. Bromberg, D. Stigter, *Molecular Driving Forces: Statistical Thermodynamics in Biology, Chemistry, Physics, and Nanoscience*, Garland Science, NY **2010**.
[31] D. Navarro-Orozco, J. C. Sánchez-Manso, *StatPearls [Internet]*, StatPearls Publishing, Tampa, Florida **2021**.
[32] A. D. Grief, G. Richardson, *J. Magn. Magn. Mater.* **2005**, *293*, 455.
[33] G. Johnson, H. Borovetz, J. Anderson, *J. Biomech.* **1992**, *25*, 91.
[34] H. Xie, M. Sun, X. Fan, Z. Lin, W. Chen, L. Wang, L. Dong, Q. He, *Sci. Rob.* **2019**, *4*, eaav8006.
[35] S. Yang, Q. Wang, D. Jin, X. Du, L. Zhang, *ACS Nano* **2022**, *16*, 19025.
[36] J. Law, X. Wang, M. Luo, L. Xin, X. Du, W. Dou, T. Wang, G. Shan, Y. Wang, P. Song, *Sci. Adv.* **2022**, *8*, eabm5752.
[37] M. P. Bui, T.-A. Le, J. Yoon, *IEEE Trans. Ind. Electron.* **2020**, *68*, 12493.
[38] Q. Wang, L. Zhang, *IEEE Open J. Nanotechnol.* **2020**, *1*, 6.
[39] C. E. Sing, L. Schmid, M. F. Schneider, T. Franke, A. Alexander-Katz, *Proc. Natl. Acad. Sci.* **2010**, *107*, 535.
[40] P. M. Boyle, T. Zghaib, S. Zahid, R. L. Ali, D. Deng, W. H. Franceschi, J. B. Hakim, M. J. Murphy, A. Prakosa, S. L. Zimmerman, *Nat. Biomed. Eng.* **2019**, *3*, 870.
[41] K. Ivanov, M. Kalinina, Y. I. Levkovich, *Microvasc. Res.* **1981**, *22*, 143.
[42] C. Alexiou, D. Diehl, P. Henninger, H. Iro, R. Rockelein, W. Schmidt, H. Weber, *IEEE Trans. Appl. Supercond.* **2006**, *16*, 1527.
[43] M. Abbas, M. N. Islam, B. P. Rao, T. Ogawa, M. Takahashi, C. Kim, *Mater. Lett.* **2013**, *91*, 326.
[44] R. Shipley, D. Gregg, *Am. J. Physiol. Legacy Content* **1944**, *141*, 289.
[45] M. E. Ibele, P. E. Lammert, V. H. Crespi, A. Sen, *ACS Nano* **2010**, *4*, 4845.
[46] H. Bruus, *Lab Chip* **2012**, *12*, 1014.
[47] T. Tasci, P. Herson, K. Neeves, D. Marr, *Nat. Commun.* **2016**, *7*, 10225.
[48] B. Yigit, Y. Alapan, M. Sitti, *Adv. Sci.* **2019**, *6*, 1801837.
[49] K. Yang, C. Lu, X. Zhao, R. Kawamura, *PLoS One* **2017**, *12*, e0188015.
[50] G. G. De La Cruz, P. Rodríguez-Fragoso, J. Reyes-Esparza, A. Rodróguez-López, R. Gómez-Cansino, L. Rodriguez-Fragoso, *Unraveling the Safety Profile of Nanoscale Particles and Materials-From Biomedical to Environmental Applications*, IntechOpen, London **2018**.
[51] D. Garzón, L. H. Camargo, D. J. Rodríguez, *J. Phys. Conf. Ser.* **2021**, *2090*, 012051.
[52] J. Takács, *COMPEL Int. J. Comput. Math. Electr. Electron. Eng.* **2001**, *20*, 1002.
[53] O. Kwon, M. Krishnamoorthy, Y. I. Cho, J. M. Sankovic, R. K. Banerjee, *J. Biomech. Eng.* **2008**, *130*, 011003.
[54] X. Zhang, T.-A. Le, A. K. Hoshiar, J. Yoon, *IEEE/ASME Trans. Mechatron.*1573.